

# Light dark matter constraints from SuperCDMS HVeV detectors operated underground with an anticoincidence event selection

M. F. Albakry,<sup>1,2</sup> I. Alkhatib,<sup>3</sup> D. Alonso-González,<sup>4,5</sup> D. W. P. Amaral,<sup>6</sup> J. Anczarski,<sup>7</sup> T. Aralis<sup>7,\*</sup> T. Aramaki,<sup>8</sup> I. J. Arnquist,<sup>9</sup> I. Ataee Langroudy,<sup>10</sup> E. Azadbakht,<sup>10</sup> C. Bathurst,<sup>11</sup> R. Bhattacharyya,<sup>10</sup> A. J. Biffl,<sup>12</sup> P. L. Brink,<sup>7</sup> M. Buchanan,<sup>3</sup> R. Bunker,<sup>9</sup> B. Cabrera,<sup>13</sup> R. Calkins,<sup>14</sup> R. A. Cameron,<sup>7</sup> C. Cartaro,<sup>7</sup> D. G. Cerdeño,<sup>4,5</sup> Y.-Y. Chang,<sup>15</sup> M. Chaudhuri,<sup>16</sup> J.-H. Chen,<sup>10</sup> R. Chen,<sup>17</sup> N. Chott,<sup>18</sup> J. Cooley,<sup>19,14</sup> H. Coombes,<sup>11</sup> P. Cushman,<sup>20</sup> R. Cyna,<sup>3</sup> S. Das,<sup>16</sup> F. De Brienne,<sup>21</sup> S. Dharani,<sup>22,23</sup> M. L. di Vacri,<sup>9</sup> M. D. Diamond,<sup>3</sup> M. Elwan,<sup>11</sup> E. Fascione,<sup>24,2</sup> E. Figueroa-Feliciano,<sup>17</sup> K. Fouts,<sup>7</sup> M. Fritts,<sup>20</sup> R. Germond,<sup>24,2</sup> M. Ghaith,<sup>25</sup> S. R. Golwala,<sup>26</sup> J. Hall,<sup>19,27</sup> S. A. S. Harms,<sup>3</sup> K. Harris,<sup>12</sup> N. Hassan,<sup>21</sup> Z. Hong,<sup>3</sup> E. W. Hoppe,<sup>9</sup> L. Hsu,<sup>28</sup> M. E. Huber,<sup>12,29</sup> V. Iyer,<sup>3</sup> D. Jardin,<sup>17</sup> V. K. S. Kashyap,<sup>16</sup> S. T. D. Keller,<sup>3</sup> M. H. Kelsey,<sup>10</sup> K. T. Kennard,<sup>17</sup> A. Kubik,<sup>19</sup> N. A. Kurinsky,<sup>7</sup> M. Lee,<sup>10</sup> J. Leyva,<sup>8</sup> J. Liu,<sup>14</sup> Y. Liu,<sup>2</sup> B. Loer,<sup>9</sup> E. Lopez Asamar,<sup>4,5</sup> P. Lukens,<sup>28</sup> D. B. MacFarlane,<sup>7</sup> R. Mahapatra,<sup>10</sup> J. S. Mammo,<sup>30</sup> N. Mast,<sup>20</sup> A. J. Mayer,<sup>2</sup> H. Meyer zu Theenhausen,<sup>22</sup> É. Michaud,<sup>21</sup> E. Michielin,<sup>22</sup> N. Mirabolfathi,<sup>10</sup> M. Mirzakhani,<sup>10</sup> B. Mohanty,<sup>16</sup> D. Monteiro,<sup>10</sup> J. Nelson,<sup>20</sup> H. Neog,<sup>20</sup> V. Novati,<sup>17</sup> J. L. Orrell,<sup>9</sup> M. D. Osborne,<sup>10</sup> S. M. Oser,<sup>1,2</sup> L. Pandey,<sup>30</sup> S. Pandey,<sup>20</sup> R. Partridge,<sup>7</sup> D. S. Pedreros,<sup>21</sup> W. Peng,<sup>3</sup> L. Perna,<sup>3</sup> W. L. Perry,<sup>3</sup> R. Podviianiuk,<sup>30</sup> S. S. Poudel,<sup>9</sup> A. Pradeep,<sup>1,2</sup> M. Pyle,<sup>15,31</sup> W. Rau,<sup>2</sup> E. Reid,<sup>6</sup> R. Ren,<sup>17</sup> T. Reynolds,<sup>3</sup> M. Rios,<sup>4,5</sup> A. Roberts,<sup>12</sup> A. E. Robinson,<sup>21</sup> J. L. Ryan,<sup>7</sup> T. Saab,<sup>11</sup> D. Sadek,<sup>11</sup> B. Sadoulet,<sup>15,31</sup> S. P. Sahoo,<sup>10</sup> I. Saikia,<sup>14</sup> J. Sander,<sup>30</sup> A. Sattari,<sup>3</sup> B. Schmidt,<sup>17</sup> R. W. Schnee,<sup>18</sup> S. Scorza,<sup>19,27</sup> B. Serfass,<sup>15</sup> A. Simchony,<sup>7</sup> D. J. Sincavage,<sup>20</sup> P. Sinervo,<sup>3</sup> J. Street,<sup>18</sup> H. Sun,<sup>11</sup> E. Tanner,<sup>20</sup> G. D. Terry,<sup>30</sup> D. Toback,<sup>10</sup> S. Verma,<sup>10</sup> A. N. Villano,<sup>12</sup> B. von Krosigk,<sup>22</sup> S. L. Watkins,<sup>15</sup> O. Wen,<sup>26</sup> Z. Williams,<sup>20</sup> M. J. Wilson,<sup>22</sup> J. Winchell,<sup>10</sup> K. Wykoff,<sup>18</sup> S. Yellin,<sup>13</sup> B. A. Young,<sup>32</sup> T. C. Yu,<sup>7</sup> B. Zatschler,<sup>19,3</sup> S. Zatschler,<sup>19,3</sup> A. Zaytsev,<sup>22,†</sup> E. Zhang,<sup>3</sup> L. Zheng,<sup>10</sup> A. Zuniga,<sup>3</sup> and M. J. Zurewski<sup>3</sup>

<sup>1</sup>Department of Physics and Astronomy, University of British Columbia, Vancouver, British Columbia V6T 1Z1, Canada

<sup>2</sup>TRIUMF, Vancouver, British Columbia V6T 2A3, Canada

<sup>3</sup>Department of Physics, University of Toronto, Toronto, Ontario M5S 1A7, Canada

<sup>4</sup>Departamento de Física Teórica, Universidad Autónoma de Madrid, 28049 Madrid, Spain

<sup>5</sup>Instituto de Física Teórica UAM-CSIC, Campus de Cantoblanco, 28049 Madrid, Spain

<sup>6</sup>Department of Physics, Durham University, Durham DH1 3LE, United Kingdom

<sup>7</sup>SLAC National Accelerator Laboratory/Kavli Institute for Particle Astrophysics and Cosmology, Menlo Park, California 94025, USA

<sup>8</sup>Department of Physics, Northeastern University, 360 Huntington Avenue, Boston, Massachusetts 02115, USA

<sup>9</sup>Pacific Northwest National Laboratory, Richland, Washington 99352, USA

<sup>10</sup>Department of Physics and Astronomy, and the Mitchell Institute for Fundamental Physics and Astronomy, Texas A&M University, College Station, Texas 77843, USA

<sup>11</sup>Department of Physics, University of Florida, Gainesville, Florida 32611, USA

<sup>12</sup>Department of Physics, University of Colorado Denver, Denver, Colorado 80217, USA

<sup>13</sup>Department of Physics, Stanford University, Stanford, California 94305, USA

<sup>14</sup>Department of Physics, Southern Methodist University, Dallas, Texas 75275, USA

<sup>15</sup>Department of Physics, University of California, Berkeley, California 94720, USA

<sup>16</sup>School of Physical Sciences, National Institute of Science Education and Research, HBNI, Jatni 752050, India

<sup>17</sup>Department of Physics and Astronomy, Northwestern University, Evanston, Illinois 60208-3112, USA

<sup>18</sup>Department of Physics, South Dakota School of Mines and Technology, Rapid City, South Dakota 57701, USA

<sup>19</sup>SNOLAB, Creighton Mine No. 9, 1039 Regional Road 24, Sudbury, Ontario P3Y 1N2, Canada

<sup>20</sup>School of Physics and Astronomy, University of Minnesota, Minneapolis, Minnesota 55455, USA

<sup>21</sup>Département de Physique, Université de Montréal, Montréal, Québec H3C 3J7, Canada

<sup>22</sup>Institute for Astroparticle Physics (IAP), Karlsruhe Institute of Technology (KIT), 76344 Eggenstein-Leopoldshafen, Germany

<sup>23</sup>Institut für Experimentalphysik, Universität Hamburg, 22761 Hamburg, Germany

<sup>24</sup>Department of Physics, Queen's University, Kingston, Ontario K7L 3N6, Canada

<sup>25</sup>College of Natural and Health Sciences, Zayed University, Dubai, 19282, United Arab Emirates

<sup>26</sup>Division of Physics, Mathematics, and Astronomy, California Institute of Technology, Pasadena, California 91125, USA

<sup>27</sup>Laurentian University, Department of Physics, 935 Ramsey Lake Road, Sudbury, Ontario P3E 2C6, Canada

<sup>28</sup>Fermi National Accelerator Laboratory, Batavia, Illinois 60510, USA

<sup>29</sup>Department of Electrical Engineering, University of Colorado Denver, Denver, Colorado 80217, USA

<sup>30</sup>Department of Physics, University of South Dakota, Vermillion, South Dakota 57069, USA

<sup>31</sup>Lawrence Berkeley National Laboratory, Berkeley, California 94720, USA

<sup>32</sup>Department of Physics, Santa Clara University, Santa Clara, California 95053, USA



(Received 31 July 2024; accepted 20 December 2024; published 15 January 2025)

This article presents constraints on dark-matter-electron interactions obtained from the first underground data-taking campaign with multiple SuperCDMS HVeV detectors operated in the same housing. An exposure of 7.63 g-days is used to set upper limits on the dark-matter-electron scattering cross section for dark matter masses between 0.5 and 1000 MeV/ $c^2$ , as well as upper limits on dark photon kinetic mixing and axionlike particle axioelectric coupling for masses between 1.2 and 23.3 eV/ $c^2$ . Compared to an earlier HVeV search, sensitivity was improved as a result of an increased overburden of 225 meters of water equivalent, an anticoincidence event selection, and better pile-up rejection. In the case of dark-matter-electron scattering via a heavy mediator, an improvement by up to a factor of 25 in cross section sensitivity was achieved.

DOI: [10.1103/PhysRevD.111.012006](https://doi.org/10.1103/PhysRevD.111.012006)

## I. INTRODUCTION

As the long-standing weakly interacting massive particle paradigm of dark matter (DM) has become increasingly constrained by experimental results, well motivated sub-GeV DM models have gained more focus [1]. Such light DM models introduce a new gauge boson that either serves as a force mediator between thermal DM and Standard Model particles or comprises the relic DM abundance on its own. Experimentally, the former can be detected via DM-electron scattering and the latter via electron absorption processes [2].

SuperCDMS high-voltage eV-resolution (HVeV) detectors use the Neganov-Trofimov-Luke (NTL) effect [3,4] to detect electron interaction energies as low as the band gap energy of silicon (Si). In the previous above-ground DM searches with HVeV detectors, constraints on the DM-electron scattering cross section, the dark photon kinetic mixing, and the axioelectric coupling of axionlike particles (ALPs) were obtained [5,6]. The limiting factor for the DM sensitivity in these searches was the excess of background events, presumably caused by luminescence of materials in the detector holder [7].

In this work, we analyze data from the first underground HVeV DM search, where the underground location reduced the rate of cosmogenic background events. To further reduce background from external sources, we operated multiple HVeV detectors in the same housing and applied an anticoincidence event selection. These changes allowed us to improve upon the DM-electron interaction constraints obtained in the previous HVeV experiments.

## II. EXPERIMENTAL SETUP

The data for this analysis were acquired at the Northwestern Experimental Underground Site (NEXUS) at Fermilab during January and February 2021 (also referred to as HVeV Run 3). The NEXUS facility provides 225 meters of water equivalent rock overburden [8]. Detectors were operated in a dilution refrigerator with dedicated lead shielding to reduce the radioactive background from the cavern where NEXUS is located. A light-tight copper housing containing the detector payload was thermally coupled to the mixing chamber of the cryostat. The temperature of the mixing chamber was stabilized at 10.5 mK throughout the run.

The detector payload consisted of four SuperCDMS HVeV detectors: one identical to the detector used in Ref. [6] and described in detail in Ref. [9] (labeled NF-C), two similar detectors with different QET<sup>1</sup> configurations (labeled NF-H and NF-F), and one identical to the detector used in Ref. [5] (labeled R1). Data from the NF-F detector were not used since a flaw in its sensor layout was discovered that prevented it from being operated properly. Each detector was fabricated on a 0.93 g high-purity Si wafer ( $10 \times 10 \times 4$  mm<sup>3</sup>). Two concentric square phonon-sensing QET channels of equal areas covered one side of each detector. A voltage differential of  $V_{\text{bias}} = 100$  V was applied between each detector's QET-bearing surface and the opposing surface to induce NTL amplification.

As shown in Fig. 1, the detectors were mounted in pairs on two copper holders, with R1 and NF-C on one holder, and NF-F and NF-H on the other. Each detector was clamped between two printed circuit boards. Only NF-C was used directly for the DM search due to its superior performance and because even with a single detector we expected the sensitivity to be limited by background rather than exposure, despite the rock overburden and anticoincidence selection. NF-H and R1

\*Contact author: taralis@slac.stanford.edu

†Contact author: azaytsev.phys@gmail.com

Published by the American Physical Society under the terms of the [Creative Commons Attribution 4.0 International](https://creativecommons.org/licenses/by/4.0/) license. Further distribution of this work must maintain attribution to the author(s) and the published article's title, journal citation, and DOI. Funded by SCOAP<sup>3</sup>.

<sup>1</sup>Quasiparticle-trap-assisted Electrothermal-feedback Transition-Edge Sensor [10].

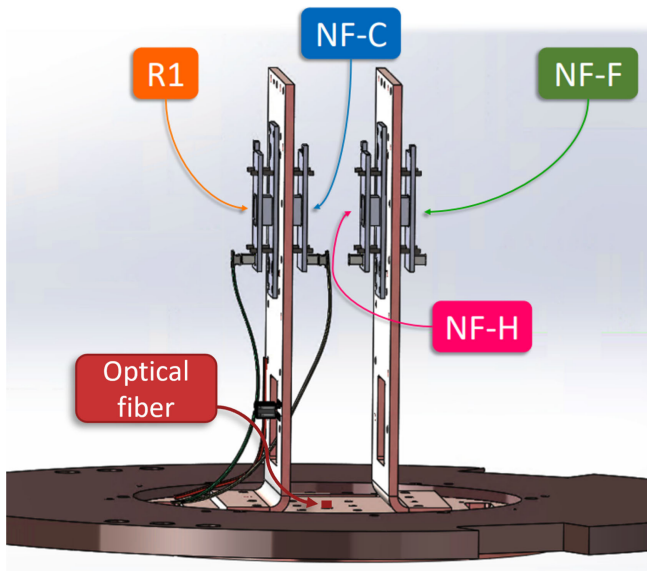


FIG. 1. Illustration of the detector setup. Four HVeV detectors were mounted on two copper holders that were thermally anchored to the mixing chamber of a dilution refrigerator. Each detector was clamped between two printed circuit boards. An optical fiber coupled to the laser diode was inserted between the detector holders. Individual MDM25 connectors were used with each detector. The associated readout cables are shown for R1 and NF-C.

served as anticoincidence detectors, as described in Sec. IV.

The detectors were read out using a SuperCDMS Detector Control and Readout Card with 625 kHz sampling frequency. Data were acquired in 0.5-second-long intervals without online triggering. Due to Detector Control and Readout Card limitations on data throughput, these intervals were separated by dead-time intervals of random lengths between 0 and 1 s, resulting in an overall dead time of 50%. An offline trigger was applied later, as described in Sec. III. In total, 13.14 days of DM-search data were collected during the run. The full data sample was used to define the event selections described in Sec. IV, but only 10% of the sample was used to define specific parameters that could have introduced subjective bias into the analysis described in Sec. VI.

As in the previous HVeV operations, a 1.95 eV laser diode was used as a source of calibration events. Photons from the laser were transmitted into the detector housing through an infrared filter and an optical fiber inserted into the bottom of the housing between the detector holders. Several calibration datasets with varied laser intensity were acquired throughout the run.

### III. EVENT RECONSTRUCTION AND CALIBRATION

To identify and characterize energy depositions, we summed together the QET currents in a given detector's

inner and outer channels after correcting for differences in the channels' responsivities. We then applied a Gaussian derivative filter, defined as a convolution with the first derivative of a Gaussian-shaped signal. A trigger threshold corresponding to  $\sim 25\%$  of the energy produced by a single  $e^-h^+$  pair was then applied to the filtered signals in NF-C and NF-H. In the case of R1, the threshold was set to  $\sim 50\%$  of the energy produced by a single  $e^-h^+$  pair due to the higher noise level observed in this detector. Trigger times were corrected using a constant time offset to approximately correspond to the rising edge of the unfiltered pulse. Time windows spanning  $\pm 6.55$  ms around each corrected trigger point were further processed to identify the amplitude of each pulse.

Pulse amplitudes and frequency-domain goodness of fit  $\chi^2$  values were calculated with the optimal filter (OF) algorithm [11]. The OF pulse template for each detector was constructed by averaging pulses from the laser calibration data. Templates had rise and fall times of  $\sim 10$   $\mu$ s and  $\sim 50$ – $150$   $\mu$ s, respectively. The noise power spectral density used in the OF to optimally weight the signal frequency components was calculated separately for each minute of data to mitigate the effect of a changing noise environment. When solving the OF  $\chi^2$  minimization problem, the template was allowed to move around the trigger point within  $\pm 15$  time samples ( $\pm 24$   $\mu$ s) to eliminate any remaining trigger misalignment.

In addition to the standard OF template fit, we performed a pileup OF fit to each triggered event [12]. This OF variant simultaneously fits the sum of two otherwise identical templates with independent amplitudes and variable time shifts. One time shift was limited to be within  $\pm 250$  time samples ( $\pm 400$   $\mu$ s) of the trigger point. The other time shift was limited to be within  $\pm 250$  time samples of the first. The  $\chi^2$  values of these fits were used to identify pileup events as described in the next section.

As in Ref. [6], we calibrated OF fit amplitudes to event energies using the alignment of laser-data  $e^-h^+$  pair peaks in the QET current distributions with their expected energies:

$$E_n = n(1.95 \text{ eV} + eV_{\text{bias}}) + E_0, \quad (1)$$

where  $n$  is the number of photons hitting the detector each producing one  $e^-h^+$  pair, 1.95 eV is the photon energy,  $e$  is the absolute electron charge, and  $V_{\text{bias}}$  is the bias voltage. The energy of the 0  $e^-h^+$  pair peak ( $E_0$ ) was measured for each laser dataset and included in Eq. (1) as offset. This offset comes from the deposition of energy that is not related to the production of  $e^-h^+$  pairs. We set the energy region of interest (ROI) for this analysis to a range that covers the first four  $e^-h^+$  pair peaks, 50–440 eV, as this range was found to be most sensitive to sub-GeV DM-electron recoil interactions in a preliminary sensitivity study.



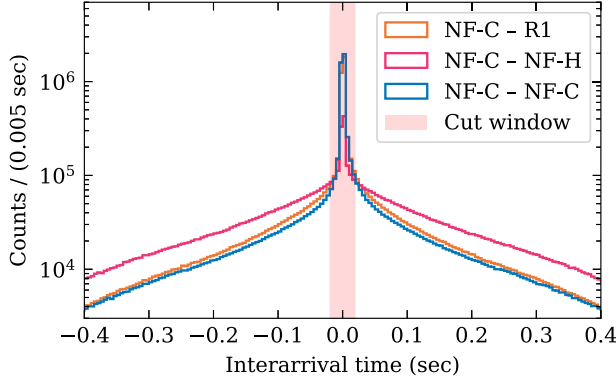


FIG. 2. Distributions of time intervals from each triggered event in NF-C (reference event) to the closest-in-time events in R1 (orange), NF-H (pink), or NF-C (blue). The values are positive (negative) when the reference event is after (before) the closest event in the respective detector. Strong time correlations are observed as sharp peaks around zero seconds. The red-shaded window shows the  $\pm 20$  ms window excluded by the anticoincidence live-time selection.

#### IV. DATA SELECTION

DM events are expected to be random and independent of each other, therefore the times between DM events occurring in a single detector are expected to follow an exponential distribution. Moreover, due to the low expected interaction cross sections, the probability of the same DM particle interacting in multiple detectors is negligible (or zero for the absorption models). Therefore, the time intervals between DM events in different detectors are also expected to follow an exponential distribution. However, as shown in Fig. 2, the distribution of interarrival times of events occurring in NF-C, as well as the distributions of time intervals between events in NF-C and the closest-in-time events in the other two detectors, contain sharp peaks around 0 s indicating events correlated in time that are inconsistent with DM candidates. We remove such correlated events by rejecting events in any detector that fall within 20-ms-long windows before and after each event. This ensures that events less than 20 ms apart are excluded from the analysis and the respective live time is removed, regardless of whether the events occurred in the same or different detectors. The choice of 20 ms was made to remove the majority of correlated events, while minimizing the loss of live time. This anticoincidence selection removed 22.9% of the total live time, while reducing the rate of events creating more than one  $e^-h^+$  pair by an order of magnitude.

In addition to the anticoincidence live-time selection, live-time selections based on the stability of temperature and the QET current baseline were applied to ensure energy amplification stability. The remaining live time after applying all the selection criteria amounted to 9.12 days. Taking into account the mass of the NF-C detector (0.93 g)

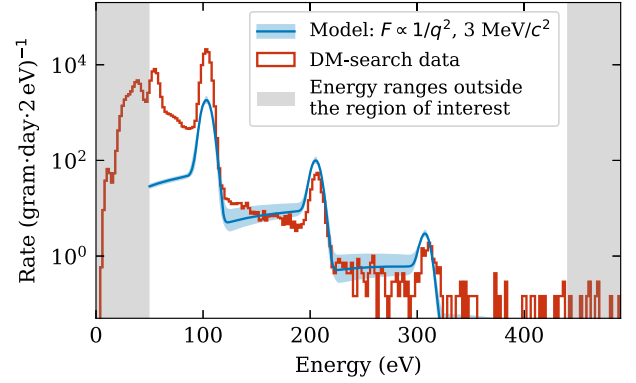


FIG. 3. The red curve shows the event rate for the dark-matter search data after live-time and event-based data selection, corrected by the selection efficiency. The blue curve shows an example of a dark-matter-electron recoil signal model for the case of  $3 \text{ MeV}c^{-2}$  dark matter interacting via an ultralight mediator (form factor  $F \propto 1/q^2$ ). The signal model is shown for the cross section value corresponding to the 90% confidence level limit produced in this work. The blue-shaded area shows the systematic uncertainties on the signal model dominated by the impact ionization uncertainty (see Sec. V). The gray-shaded regions mark the energy ranges outside the region of interest.

and the fact that only 90% of the data are used for the limit setting, the DM-search exposure was 7.63 g-days.

To remove poorly reconstructed events, we applied two selection criteria based on the OF fit quality. One selection criterion was based on the  $\chi^2$  value of the one-pulse OF fit, while the other was based on the difference between the  $\chi^2$  values of the one-pulse and two-pulse OF fits. The former criterion rejects events with pulses that have shapes deviating from the pulse template, while the latter is especially effective at rejecting events with overlapping pulses. Both criteria were developed using the laser calibration data in a way that ensures an energy-independent selection efficiency of 95%. When both criteria were applied, the selection efficiency was measured to be 90% for all events in the energy ROI.

Figure 3 shows the DM-search-data energy spectrum with the live-time and event-based selections applied, corrected by the selection efficiency. Three  $e^-h^+$ -pair peaks are visible in the spectrum, with several more peaks below the first  $e^-h^+$ -pair peak, which is located at  $\sim 100$  eV. One hypothesized explanation for the sub- $e^-h^+$  peaks is charge trapping on the sidewalls of the detector; however, further studies are required to better understand the exact origin of these events.

#### V. DARK MATTER SIGNAL MODELS

We used the resulting energy spectrum to set exclusion limits on various DM model parameters. We used the DM-electron scattering model described in Ref. [1] to set limits on the effective DM-electron cross section ( $\bar{\sigma}_e$ ), and

we used the dark-photon and ALP models described in Ref. [13] to set limits on the kinetic mixing parameter ( $\epsilon$ ) and axioelectric coupling constant ( $g_{ae}$ ).

For each model, we assumed a local DM density of  $0.3 \text{ GeV c}^{-2} \text{ cm}^{-3}$  that exclusively consisted of the candidate particle. For DM-electron scattering, we assumed the DM velocity distribution described in Ref. [14]. Specifically, we used the average DM velocity in the galactic frame of  $238.0 \text{ km/s}$  and the galactic escape velocity of  $544.0 \text{ km/s}$ . We also calculated the average Earth velocity (with respect to the DM halo) of  $253.7 \text{ km/s}$  using the average DM velocity in the galactic frame, the solar peculiar velocity, and the year-averaged velocity of Earth with respect to the Sun from Ref. [14].

The dark photon and ALP rates from Ref. [13] are proportional to the real part of the complex conductivity ( $\sigma_1$ ) of the target material. As was done for Ref. [6], we write  $\sigma_1$  in terms of the photoelectric absorption cross section ( $\sigma_{pe}$ ), the real index of refraction of Si ( $n_{Si}$ ), and the density of Si ( $\rho_{Si}$ ):

$$\sigma_1 = n_{Si} \sigma_{pe} \rho_{Si}. \quad (2)$$

For this analysis, we used  $\sigma_{pe}$  from Refs. [15–18] with the specific reference dependent on the absorption energy. We used the Si band gap energy ( $E_{gap}$ ) of  $1.131 \text{ eV}$ , calculated by performing a revised fitting of the data in Ref. [15] in order to properly account for the uncertainties in the  $\sigma_{pe}$  model (further details can be found in Appendix A).

For the Si index of refraction  $n_{Si}$ , we used the energy dependent values from Ref. [16]. Note that in the previous HVEV analysis [6], we used Ref. [19] for the ALP absorption model in which  $n_{Si} = 1$  is assumed. To correct for this difference when comparing the limits on the axioelectric coupling  $g_{ae}$ , we divided the limit from Ref. [6] by the square root of  $n_{Si}$ , as for a fixed ALP absorption rate,  $g_{ae}^2$  is inversely proportional to  $\sigma_1$ , which is in turn proportional to  $n_{Si}$  [13].

The total phonon energy measured for an event ( $E_{ph}$ ) is the recoil or absorption energy ( $E_r$ ) plus the energy produced by the NTL effect:

$$E_{ph} = E_r + n_{eh} eV_{bias}, \quad (3)$$

where  $n_{eh}$  is the number of  $e^-h^+$  pairs generated by the event. For this analysis, we used the  $e^-h^+$ -pair generation probabilities derived in Ref. [20] to compute the distribution for  $n_{eh}$  as a function of  $E_r$ . For  $E_r$  up to  $50 \text{ eV}$ , we interpolated the values provided in the supplemental materials of Ref. [20] to estimate the probabilities for  $E_{gap}$  equal to  $1.131 \text{ eV}$ . For  $E_r$  above  $50 \text{ eV}$ , we used Eqs. (13)–(15) from Ref. [20] with a small modification as described in Appendix B.

We included the following detector response effects into the signal models: bulk charge trapping (CT), bulk impact ionization (II), and energy resolution. For the bulk CT and II effects, we used the model described in Ref. [21]. The probabilities of CT and II processes to occur to a charge traversing the full thickness of the detector were obtained by fitting the model to the calibration data from Ref. [6] and were found to be  $(12.8 \pm 1.5)\%$  and  $(1.6^{+1.8}_{-1.6})\%$ , respectively.

The energy resolution was modeled as an energy-independent Gaussian smearing, with a systematic uncertainty assigned to the nominal resolution value to account for possible energy dependency. For the nominal resolution value ( $4.26 \text{ eV}$ ) we used the average between the low and high resolution estimates. The low resolution estimate ( $3.03 \text{ eV}$ ) was defined by the baseline resolution found by fitting a Gaussian to the energy distribution of randomly triggered noise events. For the high resolution estimate ( $5.49 \text{ eV}$ ) we used the Gaussian widths of the widest  $e^-h^+$  peak in the laser data within the energy ROI. The difference between the low and high estimates was used as the systematic uncertainty.

An example of a DM-electron recoil signal model with the detector response effects applied is shown in Fig. 3. The signal model shown is for a DM particle with a mass of  $3 \text{ MeV}/c^2$  scattering off of electrons via an ultralight mediator (form factor  $F \propto 1/q^2$ ). The systematic uncertainties considered are the uncertainties on the CT and II probabilities, resolution, selection efficiency and calibration. In the case of DM absorption models with particle energies  $\lesssim 3.2 \text{ eV}$ , the uncertainty on  $\sigma_{pe}$  (from measurements described in Ref. [15] and the revised fit described in Appendix A) is also taken into account.

## VI. RESULTS

We applied the same limit-setting method as in Ref. [6]. First, for each DM model and mass, we used 10% of the experimental data to estimate the upper limits on interaction strength attainable using the remaining 90% of the data. Limits were calculated by applying the Poisson counting method to events in each energy region enclosing an individual  $e^-h^+$ -pair peak. Regions were defined as  $\pm 3 \times$  the energy resolution centered on the mean energy predicted for the relevant signal model and peak. Next, for each DM model and mass, we selected the  $e^-h^+$ -pair peak expected to produce the most stringent limit. If varying the peak counts by  $\pm 1$  standard deviation indicated multiple peaks with the potential to produce the strongest limit, then we selected all such peaks. If only one peak was selected, then the final interaction strength upper limit was calculated as the 90% confidence level limit using the remaining 90% of the data. If more than one peak was selected, then the limits in each were calculated using the remaining 90% of the data with the confidence level

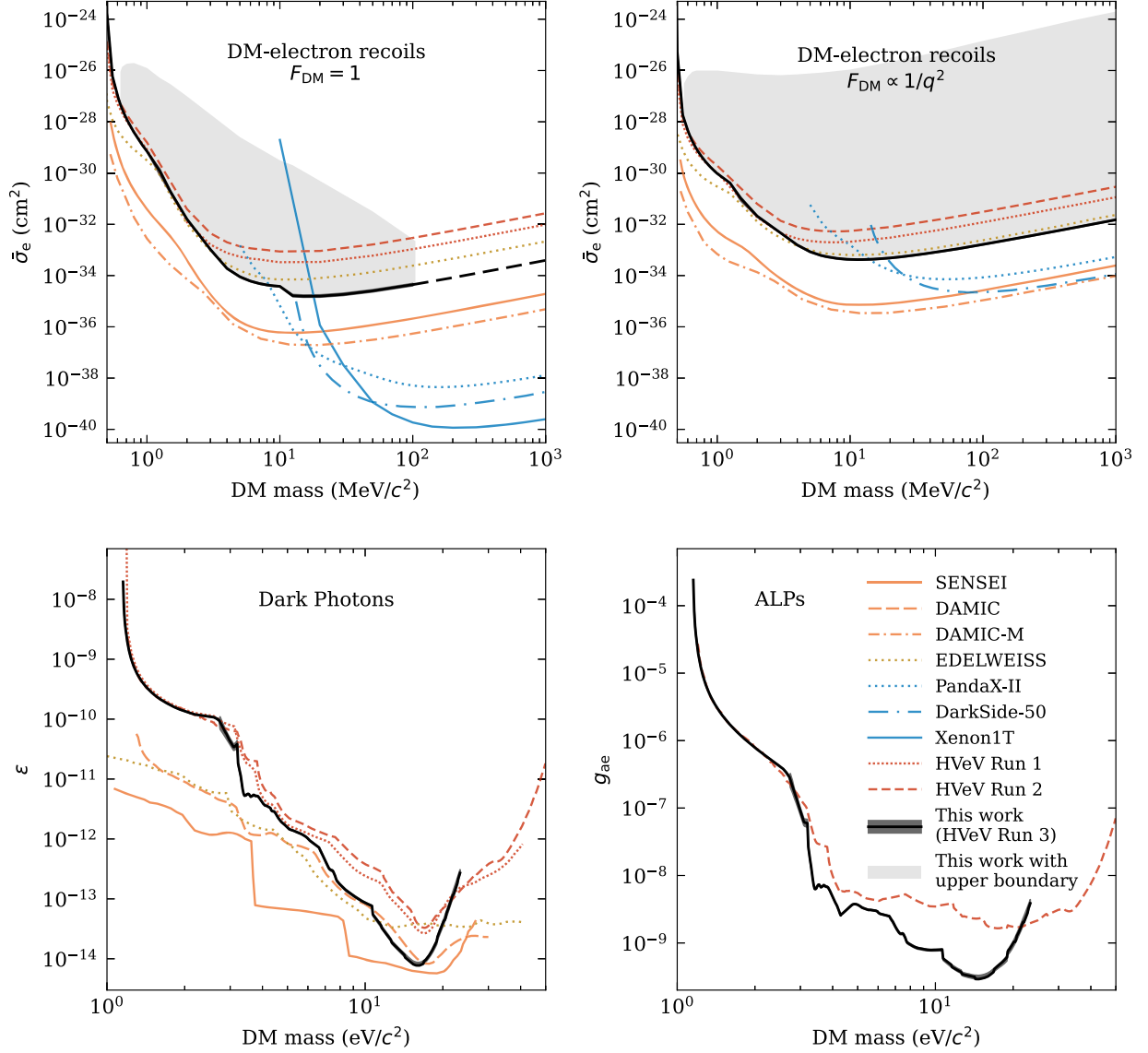


FIG. 4. 90% confidence level limits on the DM-electron recoil cross section with form-factors  $F_{\text{DM}} = 1$  (upper left) and  $F_{\text{DM}} \propto 1/q^2$  (upper right), dark photon kinetic mixing parameter (lower left) and ALP axioelectric coupling constant (lower right). Limits produced in this work are shown in black, with dark gray bands around them showing the sensitivity of the limits to systematic uncertainties (though the band is too narrow to see for most of the models and masses). In the upper plots, light gray shaded areas show the exclusion regions estimated in this work with the upper boundary arising from the Earth shielding effect. Above  $\sim 100 \text{ MeV}/c^2$ , the  $F_{\text{DM}} = 1$  limit is shown as a dashed line to indicate the predicted loss of sensitivity due to the Earth shielding effect. Other limits, shown as colored lines, are from SENSEI [22], DAMIC [23], DAMIC-M [24], EDELWEISS [25], PandaX-II [26], DarkSide-50 [27], XENON1T [28], SuperCDMS HVeV Run 1 [5], and HVeV Run 2 [6]. The HVeV Run 2 ALP limit is scaled as discussed in Sec. V.

$$C = 0.9^{1/n}, \quad (4)$$

where  $n$  is the number of selected peaks. This confidence level correction allowed us to choose the most stringent limit among the limits from the individual  $e^-h^+$ -pair peaks, producing the final 90% confidence level limit.

Systematic uncertainties were not taken into account in calculating the confidence level limits. To estimate the effect of systematic uncertainties, we varied the signal model and experimental parameters within their systematic

uncertainties, calculated limits for each variation using the method described above, and produced a band that includes 68.2% of the resulting limit variations. For all models and masses, the resulting band boundaries are within 25% of the nominal limit.

Figure 4 shows the resulting limits on the four considered DM models' signal strengths compared to the existing limits from other direct search experiments. The step in the DM-electron recoil limit with the form factor  $F_{\text{DM}} = 1$  at the mass of  $10 \text{ MeV}/c^2$  is caused by the transition from the

third to the fourth  $e^-h^+$  peak in the limit-setting procedure. Due to the use of a more limited energy ROI than the previous HVeV DM search (see Sec. III), the dark photon and ALP limits are weaker above  $\sim 20$  eV/ $c^2$  and do not extend as high in energy.

Interactions of DM particles with the Earth's atmosphere and crust attenuate the expected DM flux and change the DM velocity distribution, limiting the experiment's capacity to exclude high interaction strength values. To estimate the upper boundary of the exclusion region of the DM-electron scattering cross section, we used a Monte Carlo simulation of the Earth crust nuclear stopping power described in detail in Ref. [29] and implemented in Ref. [30]. A number of simplifications were made in this estimation: the DM flux was assumed to be directed vertically from above reaching the detector via the shortest path through the overburden, the standard continental crust composition was used (the default option in Ref. [30]), the atmosphere stopping power was ignored as subdominant [29], and lastly, the effects of CT, II, and detector resolution were ignored. Moreover, the limit-setting technique implemented in Ref. [30] is different from the one used to calculate the lower boundaries of the exclusion regions in this analysis. The Ref. [30] limit-setting energy regions are one-sided intervals above a specified threshold rather than two-sided intervals around each  $e^-h^+$ -pair peak. An older version of the Si crystal form factor is used in Ref. [30]. Additionally, no confidence level correction is included when combining Ref. [30] limits from different energy regions. Therefore, the calculated upper boundary of the exclusion region, shown in Fig. 4 as a light gray shaded area, is an approximate estimate of the Earth shielding effect ignoring various higher order effects.

One notable result of the Earth shielding effect is the predicted loss of sensitivity of our experiment to DM masses above  $\sim 100$  MeV/ $c^2$  for the heavy mediator case ( $F_{\text{DM}} = 1$ ). Because uncertainties in the Earth shielding model have not been taken into account, neither the upper boundary of the exclusion region nor the location of the sensitivity loss are conservatively estimated.

For the dark photon and ALP absorption scenarios, the upper boundaries of the parameter space exclusion regions were estimated to be above  $10^{-7}$  and  $10^{-2}$ , respectively. A more accurate calculation would require knowledge of the composition of Earth's crust and atmosphere above the NEXUS facility, including various materials' complex conductivities that are unknown for energies corresponding to the DM masses of interest.

## VII. DISCUSSION AND OUTLOOK

In the analysis presented here, the anticoincidence event selection combined with the rock overburden and improved pile-up rejection allowed us to significantly improve the exclusion limits on the DM-electron scattering cross section, dark photon kinetic mixing and ALP axioelectric

coupling compared to the previous HVeV results. The largest improvement, up to a factor of 25, is obtained for the DM-electron scattering via a heavy mediator for DM masses above 10 MeV/ $c^2$ .

The large number of background events that arrive closely spaced in time in different detectors suggests that the dominant source of background in this experiment is external, as opposed to detector internal sources such as stress-induced crystal microfractures reported in Ref. [31]. This observation is in agreement with the hypothesis introduced in Ref. [7] that suggests luminescence from printed circuit boards used in the detector holders to be a possible dominant source of background in the previous HVeV experiments. For the following HVeV run, we designed a detector holder with minimal luminescent material in order to reduce the hypothesized background. Analysis of the data collected in the run with the new holder is an ongoing effort.

## ACKNOWLEDGMENTS

We would like to thank Tongyan Lin and Tien-Tien Yu for valuable discussions of the DM signal models, Karthik Ramanathan for the help with the ionization model, and Timon Emken for the help with configuring the Earth shielding effect simulation. We gratefully acknowledge funding and support received from the National Science Foundation, the U.S. Department of Energy (DOE), Fermilab URA Visiting Scholar Grant No. 15-S-33, Natural Sciences and Engineering Research Council of Canada (NSERC), the Canada First Excellence Research Fund, the Canada Foundation for Innovation, the Arthur B. McDonald Institute (Canada), the Department of Atomic Energy Government of India (DAE), the Department of Science and Technology (DST, India), Deutsche Forschungsgemeinschaft (DFG, German Research Foundation) under Project No. 420484612 and under Germany's Excellence Strategy—EXC 2121 “Quantum Universe.” Fermilab is operated by Fermi Research Alliance, LLC, SLAC is operated by Stanford University, and PNNL is operated by the Battelle Memorial Institute for the U.S. Department of Energy under Contracts No. DE-AC02-37407CH11359, No. DE-AC02-76SF00515, and No. DE-AC05-76RL01830, respectively. This research was enabled in part by support provided by Compute Ontario [32] and the Digital Research Alliance of Canada [33]. We acknowledge the funding support provided by the Mitchell Institute at Texas A&M University to fabricate these detectors.

## APPENDIX A: REVISED PHOTOELECTRIC MODEL PARAMETERS

In Ref. [15], a temperature-dependent model of indirect photon absorption in Si was fit to newly acquired measurements of the photoelectric cross section. These



TABLE I. Variance and covariance parameters from the revised, single-stage fit of the data and indirect absorption model described in Ref. [15] to Eq. (A1).

Variance		
$\sigma_{c_0}^2$	42.6	$\text{eV}^{-4} \text{cm}^{-2}$
$\sigma_{c_1}^2$	$9.38 \times 10^{-9}$	$\text{K}^{-2}$
$\sigma_{A_2}^2$	$5.91 \times 10^6$	$\text{eV}^{-4} \text{cm}^{-2}$
$\sigma_{E_{g1}(0)}^2$	$8.50 \times 10^{-6}$	$\text{eV}^2$
Covariance		
$\sigma_{c_0} \sigma_{c_1}$	$2.67 \times 10^{-4}$	$\text{eV}^{-2} \text{cm}^{-1} \text{K}^{-1}$
$\sigma_{c_0} \sigma_{A_2}$	$-1.73 \times 10^3$	$\text{eV}^{-4} \text{cm}^{-2}$
$\sigma_{c_0} \sigma_{E_{g1}(0)}$	$1.25 \times 10^{-2}$	$\text{eV}^{-1} \text{cm}^{-1}$
$\sigma_{c_1} \sigma_{A_2}$	$-1.23 \times 10^{-2}$	$\text{eV}^{-2} \text{cm}^{-1} \text{K}^{-1}$
$\sigma_{c_1} \sigma_{E_{g1}(0)}$	$-2.97 \times 10^{-8}$	$\text{eV}^{-1} \text{K}^{-1}$
$\sigma_{A_2} \sigma_{E_{g1}(0)}$	-0.426	$\text{eV}^{-1} \text{cm}^{-1}$

measurements were made for photons with energies between 1.21 and 2.77 eV, and at four distinct temperatures between 0.5 and 295 K. An indirect absorption model with four parameters was fit to the data. The parameters were as follows: the band gap energy of the first indirect band gap  $E_{g1}(0)$ , the proportionality constant corresponding to the second indirect band gap  $A_2$ , and the coefficients  $c_0$  and  $c_1$  that parameterize the temperature-dependent proportionality constant of the first indirect band gap  $A_1(T)$ . The temperature dependence on  $A_1(T)$  is described by

$$A_1(T) = c_0 e^{-c_1 T}. \quad (\text{A1})$$

The fit procedure performed in Ref. [15] obtained the fit parameters in two steps. First, the data were fit to the model by allowing  $E_{g1}(0)$ ,  $A_2$ , and four  $A_1$  values (corresponding to the measurements taken at each temperature) to float. Next, the fit was performed again by keeping  $E_{g1}(0)$  and  $A_2$  fixed, and replacing  $A_1$  with the right side of Eq. (A1) in order to determine  $c_0$  and  $c_1$ .

The analysis performed in this work investigates the effect of systematic uncertainties on the limit result, which includes the uncertainty of the photoelectric cross section due to the indirect absorption model. This requires proper propagation of the uncertainty in the indirect absorption model using the covariance matrix of the fit parameters. However, the covariance matrix for the fit was not provided in Ref. [15]. Thus, a revised fit to the data in Ref. [15] was performed for this work to obtain the covariance matrix of the fit parameters. Here, the indirect absorption model is fit to the data in Ref. [15], where  $A_1(T)$  is again described by Eq. (A1), and the best-fit values of  $E_{g1}(0)$ ,  $A_2$ ,  $c_0$ , and  $c_1$  are obtained in one step. The results of the fit are these:  $E_{g1}(0) = 1.131(3) \text{ eV}$ ,  $A_2 = 7(2) \times 10^3 \text{ eV}^{-2} \text{cm}^{-1}$ ,  $c_0 = 321(7) \text{ eV}^{-2} \text{cm}^{-1}$ , and  $c_1 = 1.6(1) \times 10^{-3} \text{ K}^{-1}$ .

The best-fit values obtained here were used in the analysis presented in this work to compute the indirect absorption model in Si. In order to propagate the uncertainty from this model, we used the variance and covariance values obtained from the revised fit and displayed in Table I.

## APPENDIX B: IONIZATION MODEL FOR DEPOSITION ENERGIES ABOVE 50 eV

For energy depositions ( $E_r$ ) above 50 eV, the  $e^-h^+$  -pair generation probabilities were calculated using Eqs. (13)–(15) from Ref. [20]. For Eqs. (13) and (14), additional precision was provided by the paper authors. The resulting versions used for this analysis were Eqs. (B1) and (B2), respectively.  $\epsilon_{\text{eh},\infty}$  is the mean energy per electron-hole pair created for  $E_r$  above 50 eV,  $F_\infty$  is the unitless Fano factor for  $E_r$  above 50 eV, and  $A = 5.2$  is a phenomenological constant.

$$\epsilon_{\text{eh},\infty}(\text{eV}) = 1.6989 E_{\text{gap}}(\text{eV}) + 0.0843A + 1.2972, \quad (\text{B1})$$

$$F_\infty = -0.0281 E_{\text{gap}}(\text{eV}) + 0.0015A + 0.1383. \quad (\text{B2})$$

- [1] R. Essig, M. Fernández-Serra, J. Mardon, A. Soto, T. Volansky, and T.-T. Yu, *J. High Energy Phys.* **05** (2016) 046.
- [2] M. Battaglieri *et al.*, [arXiv:1707.04591](https://arxiv.org/abs/1707.04591).
- [3] B. S. Neganov and V. N. Trofimov, *Otkryt. Izobret.* **146**, 215 (1985).
- [4] P. N. Luke, *J. Appl. Phys.* **64**, 6858 (1988).
- [5] R. Agnese *et al.* (SuperCDMS Collaboration), *Phys. Rev. Lett.* **121**, 051301 (2018).

- [6] D. W. Amaral *et al.* (SuperCDMS Collaboration), *Phys. Rev. D* **102**, 091101 (2020).
- [7] M. F. Albakry *et al.* (SuperCDMS Collaboration), *Phys. Rev. D* **105**, 112006 (2022).
- [8] P. Adamson *et al.* (MINOS Collaboration), *Phys. Rev. D* **91**, 112006 (2015).
- [9] R. Ren, C. Bathurst, Y. Y. Chang, R. Chen, C. W. Fink, Z. Hong, N. A. Kurinsky, N. Mast, N. Mishra, V. Novati *et al.*, *Phys. Rev. D* **104**, 032010 (2021).



- [10] K. D. Irwin, S. W. Nam, B. Cabrera, B. Chugg, and B. A. Young, *Rev. Sci. Instrum.* **66**, 5322 (1995).
- [11] J. Wilson *et al.*, *J. Instrum.* **17**, P07010 (2022).
- [12] N. A. Kurinsky, The low-mass limit: Dark matter detectors with eV-scale energy resolution, Ph.D. thesis, Stanford University, Physics Department (2018).
- [13] Y. Hochberg, T. Lin, and K. M. Zurek, *Phys. Rev. D* **95**, 023013 (2017).
- [14] D. Baxter, I. M. Bloch, E. Bodnia, X. Chen, J. Conrad, P. Di Gangi, J. E. Y. Dobson, D. Durnford, S. J. Haselschwardt, A. Kaboth *et al.*, *Eur. Phys. J. C* **81**, 907 (2021).
- [15] C. Stanford, M. J. Wilson, B. Cabrera, M. Diamond, N. A. Kurinsky, R. A. Moffatt, F. Ponce, B. von Krosigk, and B. Young, *AIP Adv.* **11**, 025120 (2021).
- [16] D. F. Edwards, in *Handbook of Optical Constants of Solids*, edited by E. D. Palik (Academic Press, Burlington, 1997), p. 547.
- [17] B. L. Henke, E. M. Gullikson, and J. C. Davis, *At. Data Nucl. Data Tables* **54**, 181 (1993).
- [18] M. J. Berger, J. H. Hubbell, S. M. Seltzer, J. Chang, J. Coursey, R. Sukumar, D. S. Zucker, and K. Olsen, XCOM: Photon cross section database (version 1.5) (2010), [10.18434/T48G6X](https://doi.org/10.18434/T48G6X).
- [19] M. Pospelov, A. Ritz, and M. Voloshin, *Phys. Rev. D* **78**, 115012 (2008).
- [20] K. Ramanathan and N. Kurinsky, *Phys. Rev. D* **102**, 063026 (2020).
- [21] M. J. Wilson *et al.*, *Phys. Rev. D* **109**, 112018 (2024).
- [22] L. Barak *et al.* (SENSEI Collaboration), *Phys. Rev. Lett.* **125**, 171802 (2020).
- [23] A. Aguilar-Arevalo *et al.* (DAMIC Collaboration), *Phys. Rev. Lett.* **123**, 181802 (2019).
- [24] I. Arnquist *et al.* (DAMIC-M Collaboration), *Phys. Rev. Lett.* **132**, 101006 (2024).
- [25] Q. Arnaud *et al.* (EDELWEISS Collaboration), *Phys. Rev. Lett.* **125**, 141301 (2020).
- [26] C. Cheng *et al.* (PandaX-II Collaboration), *Phys. Rev. Lett.* **126**, 211803 (2021).
- [27] P. Agnes *et al.* (DarkSide Collaboration), *Phys. Rev. Lett.* **130**, 101002 (2023).
- [28] E. Aprile *et al.* (XENON Collaboration), *Phys. Rev. Lett.* **123**, 251801 (2019).
- [29] T. Emken, R. Essig, C. Kouvaris, and M. Sholapurkar, *J. Cosmol. Astropart. Phys.* **09** (2019) 070.
- [30] T. Emken, Dark Matter Simulation Code for Underground Scatterings—Crust Edition (DaMaSCUS-CRUST) (version 1.2.0) (2018), [10.5281/zenodo.2846400](https://doi.org/10.5281/zenodo.2846400).
- [31] R. Anthony-Petersen *et al.*, *Nat. Commun.* **15**, 6444 (2024).
- [32] <https://www.computeontario.ca/>
- [33] <https://alliancecan.ca/en>